



OPEN

Strain-dependent grain boundary properties of n-type germanium layers

Kota Igura^{1,3}, Koki Nozawa^{1,3}✉, Takamitsu Ishiyama^{1,2}, Takashi Suemasu¹ & Kaoru Toko¹✉

Polycrystalline Ge thin films have attracted considerable attention as potential materials for use in various electronic and optical devices. We recently developed a low-temperature solid-phase crystallization technology for a doped Ge layer and achieved the highest electron mobility in a polycrystalline Ge thin film. In this study, we investigated the effects of strain on the crystalline and electrical properties of n-type polycrystalline Ge layers. By inserting a GeO_x interlayer directly under Ge and selecting substrates with different coefficients of thermal expansion, we modulated the strain in the polycrystalline Ge layer, ranging from approximately 0.6% (tensile) to −0.8% (compressive). Compressive strain enlarged the grain size to 12 μm, but decreased the electron mobility. The temperature dependence of the electron mobility clarified that changes in the potential barrier height of the grain boundary caused this behavior. Furthermore, we revealed that the behavior of the grain boundary barrier height with respect to strain is opposite for the n- and p-types. This result strongly suggests that this phenomenon is due to the piezoelectric effect. These discoveries will provide guidelines for improving the performance of Ge devices and useful physical knowledge of various polycrystalline semiconductor thin films.

Although Ge is the oldest semiconductor used, it has once again attracted attention as its electrical and optical properties are useful for various next-generation electronics such as transistors^{1–3}, solar cells^{4,5}, optical communication^{6–8}, and thermoelectric devices^{9,10}. Particularly, there is an urgent need for a synthesis technology for Ge thin films on insulators for the following reasons: (i) although single-crystal (sc-) Ge is expensive, thinning the film can significantly reduce costs. (ii) Ge has a high optical absorption coefficient ($\sim 10^4 \text{ cm}^{-1}$ at 0.8 eV), so even a thin film can absorb sufficient light¹¹. (iii) The leakage current in transistors due to the narrow bandgap can be solved by thinning the Ge film^{3,12,13}. (iv) Owing to the low crystallization temperature and Young's modulus, it can be synthesized on general-purpose substrates, such as glass and plastic^{14–17}. Since most insulators are amorphous, Ge films synthesized directly on insulators become polycrystalline with various defects, including grain boundaries. Moreover, since the defects in Ge behave as acceptors^{18–22}, all undoped polycrystalline (poly-) Ge films exhibit p-type conduction^{23–27}. Furthermore, the activation rate of the n-type dopants in Ge is low^{28–31}. This makes it difficult to control the Fermi level, which is important in all semiconductor devices.

In recent years, it has been discovered that in the solid-phase crystallization (SPC) of Ge thin films, increasing the density of amorphous Ge precursors or adding impurities significantly affects the crystallinity of the resulting poly-Ge thin films^{32–34}. We achieved the lowest hole concentration ($2 \times 10^{16} \text{ cm}^{-3}$) for a poly-Ge thin film³⁵ and also realized control of n-type conduction by doping with impurities (Sb, As, and P)³⁶. The carrier mobility reached the highest value for a poly-Ge thin film (holes: $690 \text{ cm}^2 \text{ V}^{-1} \text{ s}^{-1}$, electrons: $450 \text{ cm}^2 \text{ V}^{-1} \text{ s}^{-1}$)^{37,38}. The best performance of a low-temperature thin film transistor using a poly-Ge layer was also demonstrated^{39,40}.

Based on these techniques, we have studied strains naturally applied to poly-Ge thin films⁴¹. The amount of strain mainly depended on the difference in the thermal expansion of the substrate. Although it was not sufficiently large to modulate the band structure of Ge⁴², it significantly affected the grain boundary barrier height (E_B) of the p-type Ge thin film. In this study, we investigate the effects of strain on the crystallinity and electrical properties of n-type Ge thin films. The strain dependence of E_B in the n-type Ge thin films was inversely correlated with that in the p-type Ge thin films. This behavior suggests that the change in E_B owing to strain is due to the piezoelectric effect^{43–46}.

¹Institute of Applied Physics, University of Tsukuba, 1-1-1 Tennodai, Tsukuba, Ibaraki 305–8573, Japan. ²JSPS Research Fellow, 8 Ichiban-cho, Chiyoda-ku, Tokyo 102–8472, Japan. ³These authors contributed equally: Kota Igura and Koki Nozawa. ✉email: noza.ez@gmail.com; toko@bk.tsukuba.ac.jp

Experimental

Various substrates with different coefficients of thermal expansion (CTEs) were used to modulate widely the strain applied to the Ge layer, including SiO₂, Si (111), CaF₂ (001), and polyimide (PI). We denote the CTE difference between Ge and substrate as $\Delta\alpha$; the values are presented in Table 1. Before thin-film deposition, the substrates were cleaned with acetone, methanol, and distilled water. We fabricated 15-nm thick GeO_x layers on the substrates using radio-frequency magnetron sputtering (base pressure: 4.0×10^{-4} Pa) at 10 sccm. Ar plasma (working pressure: 0.5 Pa) was used with the radio-frequency power set to 50 W. The GeO_x layer excluded the influence of the substrate-interface species and extracted the influence of the difference in CTEs on the Ge layer^{37,41}. The samples were then air-transferred from the sputtering chamber to a molecular beam deposition system (base pressure: 5×10^{-7} Pa) within five minutes to avoid the reaction of GeO_x with air. Subsequently, the phosphorus-doped amorphous Ge layers were prepared using a Knudsen cell with a solid Ge source (purity: 99.999%). The Ge thickness was maintained at 200 nm, with a constant Ge deposition rate of 3.4 nm min⁻¹. The phosphorus concentration in Ge was 2×10^{20} cm⁻³. The sample stage was heated at 125 °C during deposition to densify the amorphous Ge layer^{33,38}. The samples were then loaded into a conventional tube furnace (Koyo Thermo Systems, KTF035N1) with N₂ flow (purity: 99.9%, flow rate: 0.1 L min⁻¹) and annealed at 400 °C for 50 h to induce SPC. The temperature was calibrated by placing a thermocouple directly on the tube furnace and was confirmed to be uniform within the sample stage.

Optical microscopy was employed during annealing using a Linkam 10042 D microscope with Keyence VH-5500. The resulting samples were evaluated using Raman spectroscopy, atomic force microscopy (AFM), scanning electron microscopy (SEM), electron backscatter diffraction (EBSD), and Hall-effect measurements. Raman spectra were measured using a JASCO NRS-5100 with a frequency-doubled Nd:YAG laser (wavelength: 532 nm, power: 0.5 mW, spot diameter: 5 μ m), where the laser power was weak enough not to affect the crystal phase and peak shift. The penetration depth of the laser in poly-Ge was estimated to be approximately 30 nm from the absorption coefficient of Ge at the laser wavelength. The absolute Raman shift (detector resolution: 0.42 cm⁻¹) was calibrated using the transverse optical phonon line (300 cm⁻¹) of sc-Ge(100). The root mean square (RMS) values were measured by AFM using a Shimadzu SPM-9600 instrument. The SEM and EBSD were performed using a Hitachi High-Tech SU7000 instrument (voltage: 15 kV) equipped with an Oxford AZtec analysis attachment. Hall effect measurements using the Van der Pauw method were performed using an M91 FastHall and AX-2022041R with a 0.45 T permanent magnet.

Results and discussion

Figure 1a shows how strain is introduced into the Ge layer during the annealing process. During temperature rise, strain is applied to Ge according to $\Delta\alpha$. Subsequently, strain relaxation in Ge happens during the nucleation and grain growth at 400 °C as a dynamic process. During temperature reduction, strain is reintroduced into Ge according to $\Delta\alpha$, which is in the opposite direction to that applied during the temperature rise. Figure 1b shows that the Ge crystallization progresses with increasing annealing time. According to the optical

Substrate	CTE [10^{-6} K ⁻¹]	$\Delta\alpha$ [10^{-6} K ⁻¹]
SiO ₂	0.5	-5.3
Si	3.9	-1.9
CaF ₂	18.9	13.1
PI	27.0	21.2

Table 1. Coefficients of thermal expansion (CTEs) and CTE differences between Ge and substrate ($\Delta\alpha$) at room temperature.

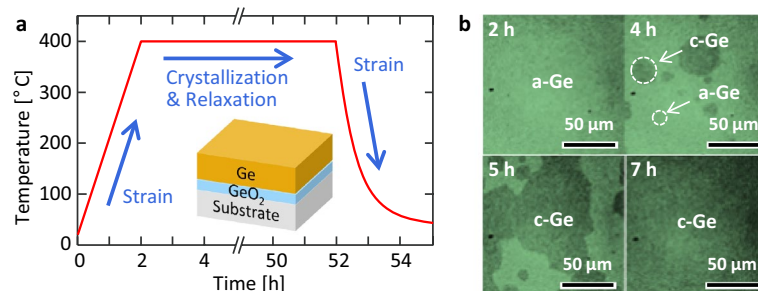


Figure 1. Annealing process of the samples. (a) Temperature profile and strain history in Ge. The inset shows the schematic of the sample structure. (b) Annealing-time evolution optical micrographs showing the crystal growth of the sample with a SiO₂ substrate. The light- and dark-colored areas indicate amorphous (a-) and crystalline (c-) Ge, respectively.

microscopy observations, crystallization was completed within 5 h at 400 °C for all samples. Therefore, the long-time annealing for 50 h would sufficiently relax the strain in Ge at 400 °C, leaving the strain only due to $\Delta\alpha$ in Ge after cooling.

As shown in Fig. 2a, a uniform mirror-like Ge film was formed in all samples. The AFM image in Fig. 2b shows that the surface of the Ge layer is flat, which is one of the advantages of SPC. The SEM image in Fig. 2c shows a contrast on the order of micrometers. When considered together with the AFM results, the contrasts in the SEM image is due to the electron channeling effect: a phenomenon in which the penetration depth of an electron beam changes depending on the crystal orientation⁴⁷. This suggests that the Ge layer has high crystallinity, which is similar in all samples.

Figure 3a shows a sharp peak around 300 cm^{-1} caused by Ge crystals in the Raman spectra of all samples. Although the full width at half maximum (FWHM) of the Ge peaks was approximately the same, the Raman shift changed depending on the sample. Figure 3b shows the peak shift ($\Delta\omega$) from the Ge peak of the sc-Ge wafer in each sample. It can be seen that as $\Delta\alpha$ becomes larger, $\Delta\omega$ becomes larger. The strain ϵ in the Ge layer is expressed as $\epsilon = \Delta\omega / b$ using the strain phonon coefficient b . The ϵ value of the Ge film on each substrate was calculated by substituting $b = -395 \text{ cm}^{-1}$, as proposed by Manganeli et al.⁴⁸. A positive ϵ corresponds to tensile strain, and a negative ϵ corresponds to compressive strain. It can be seen that tensile strain is applied when $\Delta\alpha < 0$, and compressive strain is applied when $\Delta\alpha > 0$. Furthermore, the theoretical strain ϵ_{th} obtained from $\Delta\alpha$ is shown by a dotted line defined using

$$\epsilon_{\text{th}} = \frac{\Delta\alpha \Delta T}{1-\nu}, \quad (1)$$

where ΔT is the difference between the annealing temperature (400 °C) and room temperature (300 K), and ν is the Poisson's ratio of the thin film⁴⁹. The trend of ϵ roughly matches the trend of ϵ_{th} , which indicates that the difference in CTEs with the substrate mainly causes the strain in the Ge layer. Moreover, ϵ showed a slightly higher value than ϵ_{th} in all samples. One possible reason for the difference could be that $\Delta\alpha$ was calculated as a constant, while CTE depended on temperature⁵⁰. From the above, it can be seen that a reasonable strain is applied to the Ge film in response to $\Delta\alpha$.

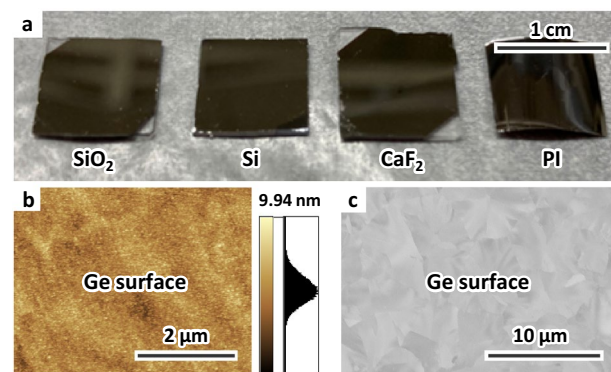


Figure 2. Sample appearance after annealing. (a) Photograph of the samples with an SiO_2 , Si, CaF_2 and PI substrate. (b) AFM and (c) SEM images of the sample with a SiO_2 substrate.

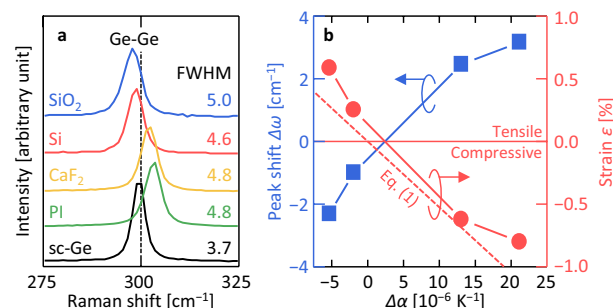


Figure 3. Raman spectroscopy analysis of the samples. (a) Raman spectra of the samples after annealing, where the crystal Ge peak position for a sc-Ge wafer is shown as a dotted line. The FWHM values of the Ge peaks are shown near each spectrum. (b) $\Delta\omega$ and ϵ as functions of $\Delta\alpha$, where $\epsilon > 0$ corresponds to tensile strain and $\epsilon < 0$ corresponds to compressive strain. The dotted line shows ϵ_{th} obtained from Eq. (1).

Figures 4a–d show inverse pole figure images of the Ge layers obtained by EBSD. A random orientation was observed in all samples, and no difference in orientation was observed depending on the substrate. This is due to the insertion of an a-GeO_x layer at the Ge/substrate interface^{37,41}. By contrast, the grain size depends on the type of substrate used. The RMS roughness of each sample was evaluated using AFM, as shown in Fig. 4e. Although the RMS roughness was similar for the samples with the SiO₂, Si, and CaF₂ substrates, it was higher for the sample with the PI substrate. Since these values are comparable to the RMS of each substrate, it can be seen that the Ge layer inherits the irregularities of the substrate. Figure 4e shows results summarizing changes in the average grain size and twin grain boundary density concerning $\Delta\alpha$. As $\Delta\alpha$ increased, the grain size increased and then decreased, while the twin grain boundary density exhibited the opposite trend. It is known that both strain and roughness in thin films affect the nucleation frequency and growth rate^{14,51–53}. The fact that the Ge grain size varied for the SiO₂, Si, and CaF₂ samples with similar roughness suggests that the strain applied to the a-Ge layer during temperature rise affects the crystal growth (Fig. 1a). Conversely, the small grains in the PI sample are explained as a pronounced interfacial inhomogeneous nucleation due to the rough substrate surface.

Figure 5a shows the results of the Hall measurements. Similar to the behavior of hole concentration in p-type Ge⁴¹, the electron concentration n was almost constant with respect to $\Delta\alpha$. Conversely, as $\Delta\alpha$ increases, the electron mobility μ decreases. Generally, μ in polycrystalline semiconductors is limited by grain boundary scattering^{54,55}, but this behavior is inconsistent with the grain size trend shown in Fig. 4. To clarify this, we calculated E_B based on the Evans and Nelson model⁵⁵, where μ is defined as

$$\mu = \frac{Lq}{k_B T} \frac{v_r}{1 + \frac{v_r}{v_d}} \exp\left(-\frac{E_B}{k_B T}\right), \quad (2)$$

where L is the grain size, q is the elementary charge, v_r is the recombination velocity, v_d is the drift–diffusion velocity, and T is the measurement temperature. Therefore, we can obtain E_B from the slope of the Arrhenius plots against μT . Figure 5b shows the Arrhenius plots for μT . It can be seen that μT decreases monotonically as a function of $1000/T$, which means that μ is limited by grain boundary scattering.

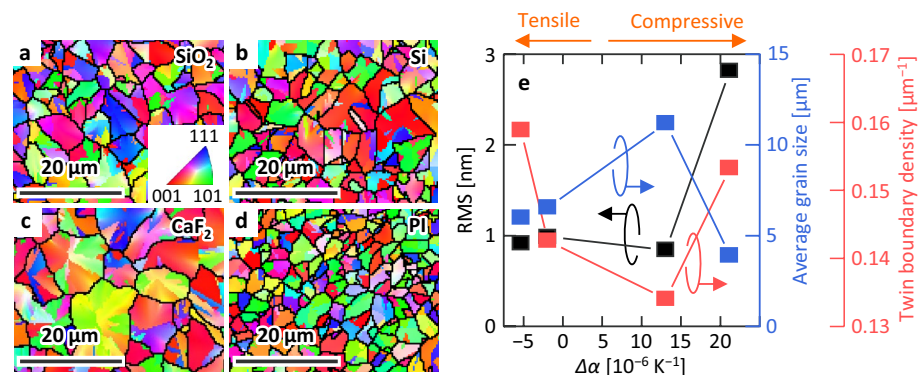


Figure 4. Crystal properties of the Ge layers. Inverse pole figure images from EBSD analyses for the samples with (a) SiO₂, (b) Si, (c) CaF₂, and (d) PI substrate. The color in crystal orientation maps indicates the crystal orientation (refer to legend in the inset). Grain boundaries are shown as black lines. (e) RMS, average grain size, and twin boundary density as a function of $\Delta\alpha$.

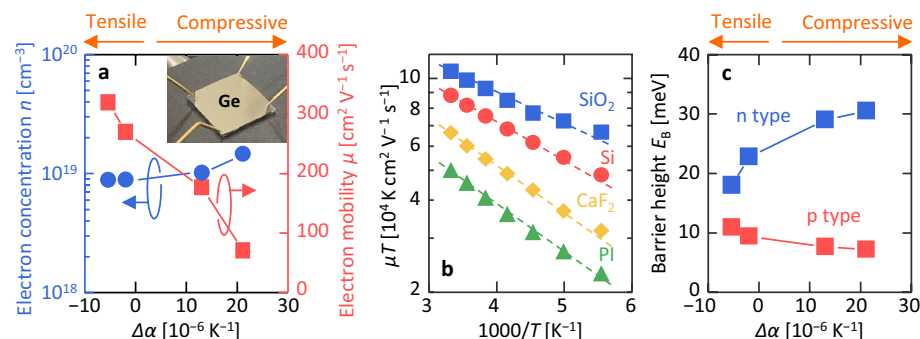


Figure 5. Electrical properties of the Ge layers. (a) n and μ as functions of $\Delta\alpha$, where the inset shows the measurement setup. (b) Arrhenius plots of μT of the samples, where the dotted lines are the fitted lines used to derive E_B . (c) E_B as a function of $\Delta\alpha$. The data of p-type Ge layers were derived by recalculating the data in Ref. 41 with the Evans and Nelson model.

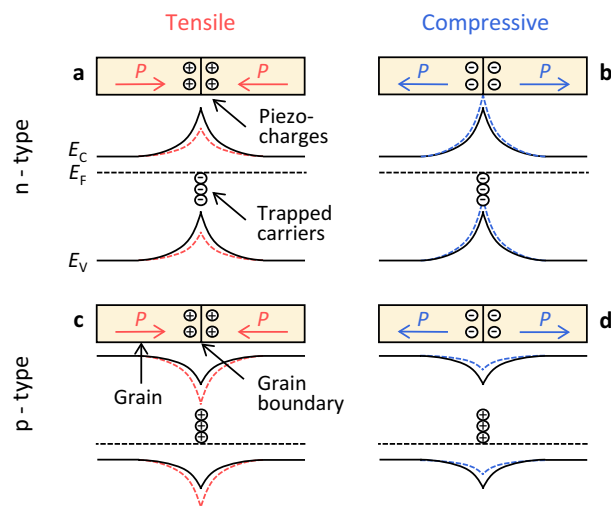


Figure 6. Strain effects on the grain boundary potential. Schematic of piezoelectric effects and band structures for the (a) tensile-strained n-type Ge, (b) compressive-strained n-type Ge, (c) tensile-strained p-type Ge, and (d) compressive-strained p-type Ge. The conduction (E_C) and valence (E_V) band curves are solid without strains and dashed with strains. P is the polarization vector generated by the strains in Ge.

Figure 5c shows the E_B calculated from the slope of the regression line indicated by the dotted line in Fig. 5b. As $\Delta\alpha$ increased, E_B clearly increased. By contrast, the E_B of a similarly prepared undoped p-type Ge layer decreased with increasing $\Delta\alpha$, as we have previously reported⁴¹. Thus, the poly-Ge layer strain significantly affects the electrical properties, especially E_B .

The fact that E_B shows the opposite behavior with strain for the n-type and p-type layers strongly suggests that piezoelectric effects cause changes in E_B ^{43–46}. Figure 6 illustrates the strain effects on the grain boundary barrier height of the Ge layer. In polycrystalline semiconductors, grain boundary defects act as carrier traps for electrons in n-type and holes in p-type, so that the Fermi level (E_F) within the grain and at the grain boundary are equal. This phenomenon forms potential barriers that prevents carrier transport. When strain is applied to a poly-Ge layer, polarization vectors (P) are generated in the grains, corresponding to strain direction. When the charge induced near the grain boundary by the polarization (piezo-charge) and the trapped carriers at the grain boundary are of different types, E_B decreases due to charge compensation (Figs. 6a,d). In contrast, when the piezo-charge and trapped carriers are the same type, E_B increases (Figs. 6b,c). Thus, the relationship between the strain and E_B in the poly-Ge layer is consistent with the piezoelectric effect, although it is still a matter of speculation.

Conclusions

We investigated the effects of the thermal strain caused by the substrate on the crystallinity and electrical properties of an n-type Ge layer. Using SiO_2 , Si, CaF_2 , and PI substrates, the amount of strain in the poly-Ge layer was modulated in the range from 0.6% to -0.8% , where positive values correspond to tensile strain, and negative values correspond to compressive strain. Compressive strain expanded the grain size, reaching approximately $12\ \mu\text{m}$ in the CaF_2 substrate sample, while decreasing μ . We derived E_B from the temperature dependence of μ and clarified that a decrease in μ is due to an increase in E_B . The behavior of E_B with strain was opposite between the n- and p-types, which strongly suggests that piezoelectric effect caused this phenomenon. These results will be crucial for controlling the properties of poly-Ge devices and various polycrystalline semiconductor thin films.

Data availability

The datasets used and/or analyzed in the current study are available from the corresponding author upon reasonable request.

Received: 7 December 2023; Accepted: 4 March 2024

Published online: 03 April 2024

References

- Saraswat, K. *et al.* High performance germanium MOSFETs. *Mater. Sci. Eng. B* **3**, 242–249 (2006).
- Brunco, D. P. *et al.* Germanium MOSFET devices: Advances in materials understanding, process development, and electrical performance. *J. Electrochem. Soc.* **155**, H552 (2008).
- Toriumi, A. & Nishimura, T. Germanium CMOS potential from material and process perspectives: Be more positive about germanium. *Jpn. J. Appl. Phys.* **57**, 010101 (2017).
- King, R. R. *et al.* 40% efficient metamorphic GaInP/GaInAs/Ge multijunction solar cells. *Appl. Phys. Lett.* **90**, 183516 (2007).
- Shahrjerdi, D. *et al.* High-efficiency thin-film InGaP/InGaAs/Ge tandem solar cells enabled by controlled spalling technology. *Appl. Phys. Lett.* **100**, 053901 (2012).
- Michel, J., Liu, J. & Kimerling, L. C. High-performance Ge-on-Si photodetectors. *Nat. Photonics* **4**, 527–534 (2010).

7. Matsue, M. *et al.* Strain-induced direct band gap shrinkage in local Ge-on-insulator structures fabricated by lateral liquid-phase epitaxy. *Appl. Phys. Lett.* **104**, 031106 (2014).
8. Kang, J., Takenaka, M. & Takagi, S. Novel Ge waveguide platform on Ge-on-insulator wafer for mid-infrared photonic integrated circuits. *Opt. Express* **24**, 11855 (2016).
9. Taniguchi, T. *et al.* Thermoelectric $\text{Si}_{1-x}\text{Ge}_x$ and Ge epitaxial films on Si(001) with controlled composition and strain for group IV element-based thermoelectric generators. *Appl. Phys. Lett.* **117**, 141602 (2020).
10. Ozawa, T., Imajo, T., Suemasu, T. & Toko, K. High thermoelectric power factors in polycrystalline germanium thin films. *Appl. Phys. Lett.* **119**, 132101 (2021).
11. Sze, S. M. *Semiconductor Devices, Physics and Technology* (Wiley, 1985).
12. Maeda, T. *et al.* Thin-body Ge-on-insulator p-channel MOSFETs with Pt germanide metal source/drain. *Thin Solid Films* **508**, 346–350 (2006).
13. Moto, K. *et al.* Polycrystalline thin-film transistors fabricated on high-mobility solid-phase-crystallized Ge on glass. *Appl. Phys. Lett.* **114**, 212107 (2019).
14. Hekmatshoar, B., Mohajerzadeh, S., Shahrjerdi, D. & Robertson, M. D. Thin-film tunneling transistors on flexible plastic substrates based on stress-assisted lateral growth of polycrystalline germanium. *Appl. Phys. Lett.* **85**, 1054–1056 (2004).
15. Wang, Z. M., Wang, J. Y., Jeurgens, L. P. H., Philipp, F. & Mittemeijer, E. J. Origins of stress development during metal-induced crystallization and layer exchange: Annealing amorphous Ge/crystalline Al bilayers. *Acta Mater.* **56**, 5047–5057 (2008).
16. Higashi, H. *et al.* A crystalline germanium flexible thin-film transistor. *Appl. Phys. Lett.* **111**, 222105 (2017).
17. Toko, K. & Suemasu, T. Metal-induced layer exchange of group IV materials. *J. Phys. D: Appl. Phys.* **53**, 373002 (2020).
18. Haesslein, H., Sielemann, R. & Zistl, C. Vacancies and Self-Interstitials in Germanium Observed by Perturbed Angular Correlation Spectroscopy. *Phys. Rev. Lett.* **80**, 2626–2629 (1998).
19. Broqvist, P., Alkauskas, A. & Pasquarello, A. Defect levels of dangling bonds in silicon and germanium through hybrid functionals. *Phys. Rev. B Condens. Matter* **78**, 075203 (2008).
20. Weber, J. R., Janotti, A. & Van de Walle, C. G. Dangling bonds and vacancies in germanium. *Phys. Rev. B Condens. Matter* **87**, 035203 (2013).
21. Shen, L. *et al.* The effect of vacancy defects on the conductive properties of SiGe. *Phys. Lett. A* **386**, 126993 (2021).
22. Imajo, T., Ishiyama, T., Nozawa, K., Suemasu, T. & Toko, K. Acceptor defects in polycrystalline Ge layers evaluated using linear regression analysis. *Sci. Rep.* **12**, 14941 (2022).
23. Toko, K., Nakao, I., Sadoh, T., Noguchi, T. & Miyao, M. Electrical properties of poly-Ge on glass substrate grown by two-step solid-phase crystallization. *Solid State Electron.* **53**, 1159–1164 (2009).
24. Tsao, C.-Y., Huang, J., Hao, X., Campbell, P. & Green, M. A. Formation of heavily boron-doped hydrogenated polycrystalline germanium thin films by co-sputtering for developing p^+ emitters of bottom cells. *Sol. Energy Mater. Sol. Cells* **95**, 981–985 (2011).
25. Jung, H.-W., Jung, W.-S., Yu, H.-Y. & Park, J.-H. Electrical properties of phosphorus-doped polycrystalline germanium formed by solid-phase and metal-induced crystallization. *J. Alloys Compd.* **561**, 231–233 (2013).
26. Usuda, K. *et al.* High-performance poly-Ge short-channel metal-oxide-semiconductor field-effect transistors formed on SiO_2 layer by flash lamp annealing. *Appl. Phys. Express* **7**, 056501 (2014).
27. Takeuchi, W. *et al.* High hole mobility tin-doped polycrystalline germanium layers formed on insulating substrates by low-temperature solid-phase crystallization. *Appl. Phys. Lett.* **107**, 022103 (2015).
28. Koike, M. *et al.* Diffusion and activation of n-type dopants in germanium. *J. Appl. Phys.* **104**, 023523 (2008).
29. Takahashi, K. *et al.* High n-type Sb dopant activation in Ge-rich poly- $\text{Ge}_{1-x}\text{Sn}_x$ layers on SiO_2 using pulsed laser annealing in flowing water. *Appl. Phys. Lett.* **112**, 062104 (2018).
30. Sgourou, E. N., Panayiotatos, Y., Vovk, R. V., Kuganathan, N. & Chronos, A. Diffusion and dopant activation in germanium: insights from recent experimental and theoretical results. *Appl. Sci.* **9**, 2454 (2019).
31. Ozawa, T., Imajo, T., Suemasu, T. & Toko, K. High thermoelectric power factors in polycrystalline germanium thin films. *Appl. Phys. Lett.* **119**, 132101 (2021).
32. Sadoh, T., Kai, Y., Matsumura, R., Moto, K. & Miyao, M. High carrier mobility of Sn-doped polycrystalline-Ge films on insulators by thickness-dependent low-temperature solid-phase crystallization. *Appl. Phys. Lett.* **109**, 232106 (2016).
33. Toko, K., Yoshimine, R., Moto, K. & Suemasu, T. High-hole mobility polycrystalline Ge on an insulator formed by controlling precursor atomic density for solid-phase crystallization. *Sci. Rep.* **7**, 16981 (2017).
34. Moto, K., Yoshimine, R., Suemasu, T. & Toko, K. Improving carrier mobility of polycrystalline Ge by Sn doping. *Sci. Rep.* **8**, 14832 (2018).
35. Mizoguchi, T. *et al.* Solid-phase crystallization of GeSn thin films on GeO_2 coated glass. *Phys. Status Solidi Rapid Res. Lett.* **16**, 2100509 (2022).
36. Nozawa, K., Nishida, T., Ishiyama, T., Suemasu, T. & Toko, K. n-Type polycrystalline germanium layers formed by impurity-doped solid-phase growth. *ACS Appl. Electron. Mater.* **5**, 1444–1450 (2023).
37. Imajo, T. *et al.* Record-high hole mobility germanium on flexible plastic with controlled interfacial reaction. *ACS Appl. Electron. Mater.* **4**, 269–275 (2022).
38. Nozawa, K. *et al.* High-electron mobility P-doped polycrystalline GeSn layers formed on insulators at low temperatures. *Appl. Phys. Lett.* **122**, 201901 (2023).
39. Moto, K. *et al.* Polycrystalline thin-film transistors fabricated on high-mobility solid-phase-crystallized Ge on glass. *Appl. Phys. Lett.* **114**, 212107 (2019).
40. Moto, K. *et al.* Sn concentration effects on polycrystalline GeSn thin film transistors. *IEEE Electron Device Lett.* **42**, 1735–1738 (2021).
41. Imajo, T., Suemasu, T. & Toko, K. Strain effects on polycrystalline germanium thin films. *Sci. Rep.* **11**, 8333 (2021).
42. Fischetti, M. V. & Laux, S. E. Band structure, deformation potentials, and carrier mobility in strained Si, Ge, and SiGe alloys. *J. Appl. Phys.* **80**, 2234 (1996).
43. Smith, C. S. Piezoresistance effect in germanium and silicon. *Phys. Rev.* **94**, 42–49 (1954).
44. Matsuda, K., Suzuki, K., Yamamura, K. & Kanda, Y. Nonlinear piezoresistance effects in silicon. *J. Appl. Phys.* **73**, 1838 (1993).
45. Wang, Z. L. & Wu, W. Piezotronics and piezo-phototronics: fundamentals and applications. *Natl. Sci. Rev.* **1**, 62–90 (2014).
46. Baraki, R. *et al.* Varistor piezotronics: Mechanically tuned conductivity in varistors. *J. Appl. Phys.* **118**, 085703 (2015).
47. Joy, D. C., Newbury, D. E. & Davidson, D. L. Electron channeling patterns in the scanning electron microscope. *J. Appl. Phys.* **53**, R81–R122 (1982).
48. Manganelli, C. L. *et al.* Temperature dependence of strain-phonon coefficient in epitaxial Ge/Si(001): A comprehensive analysis. *J. Raman Spectrosc.* **51**, 989–996 (2020).
49. Narayan, J. & Nandedkar, A. S. Atomic structure and energy of grain boundaries in silicon, germanium and diamond. *Philos. Mag. B* **63**, 1181–1192 (1991).
50. Grimvall, G. *Thermophysical Properties of Materials* (Elsevier, 1999).
51. Moniwa, M. *et al.* Preferential nucleation along SiO_2 steps in amorphous Si. *Appl. Phys. Lett.* **47**, 113–115 (1985).
52. Toko, K., Sadoh, T. & Miyao, M. Indentation-induced low-temperature solid-phase crystallization of $\text{Si}_{1-x}\text{Ge}_x$ ($x = 0-1$) on insulator. *Appl. Phys. Lett.* **94**, 192106 (2009).

53. Beena Unni, A., Winkler, R., Duarte, D. M., Chat, K. & Adrjanowicz, K. Influence of surface roughness on the dynamics and crystallization of vapor-deposited thin films. *J. Phys. Chem. B* **126**, 8072–8079 (2022).
54. Seto, J. Y. W. The electrical properties of polycrystalline silicon films. *J. Appl. Phys.* **46**, 5247–5254 (1975).
55. Evans, P. V. & Nelson, S. F. Determination of grain-boundary defect-state densities from transport measurements. *J. Appl. Phys.* **69**, 3605–3611 (1991).

Acknowledgements

This study was financially supported by the JSPS KAKENHI (No. 21H01358), JSPS Research Fellows (No. 23KJ0271), NEDO (No. P14004), and JST FOREST (No. JPMJFR222J), TEPCO Memorial Foundation, and JACI Prize for Encouraging Young Researchers. The authors are grateful to Prof. T. Sekiguchi (University of Tsukuba) for EBSD measurements. The experiments were conducted at the Advanced Research Infrastructure for Materials and Nanotechnology, Japan.

Author contributions

K.T. and K. N. conceived and designed the experiments. K. I., K. N., and T. I. performed the experiments and analyses. K.T. and T.S. managed the study and supervised the project. All the authors discussed the results and commented on the manuscript.

Competing interests

The authors declare no competing interests.

Additional information

Correspondence and requests for materials should be addressed to K.N. or K.T.

Reprints and permissions information is available at www.nature.com/reprints.

Publisher's note Springer Nature remains neutral with regard to jurisdictional claims in published maps and institutional affiliations.



Open Access This article is licensed under a Creative Commons Attribution 4.0 International License, which permits use, sharing, adaptation, distribution and reproduction in any medium or format, as long as you give appropriate credit to the original author(s) and the source, provide a link to the Creative Commons licence, and indicate if changes were made. The images or other third party material in this article are included in the article's Creative Commons licence, unless indicated otherwise in a credit line to the material. If material is not included in the article's Creative Commons licence and your intended use is not permitted by statutory regulation or exceeds the permitted use, you will need to obtain permission directly from the copyright holder. To view a copy of this licence, visit <http://creativecommons.org/licenses/by/4.0/>.

© The Author(s) 2024